Time-resolved multispectral imaging based on an adaptive single-pixel camera

Florian Rousset,[1,2,*] Nicolas Ducros,[1] Françoise Peyrin,[1] Gianluca Valentini,[2] Cosimo D'Andrea,[2,3] and Andrea Farina[4]

[1] *Univ Lyon, INSA Lyon, UCBL, CNRS 5220, INSERM U1206, CREATIS, 69621 Villeurbanne, France*
[2] *Dipartimento di Fisica, Politecnico di Milano, 20133 Milan, Italy*
[3] *Centre for Nano Science and Technology@Polimi, Istituto Italiano di Tecnologia, 20133 Milan, Italy*
[4] *Consiglio Nazionale delle Ricerche, IFN, 20133 Milan, Italy*
[*] *Florian.Rousset@creatis.insa-lyon.fr*

Abstract: Time-resolved multispectral imaging has many applications in different fields, which range from characterization of biological tissues to environmental monitoring. In particular, optical techniques, such as lidar and fluorescence lifetime imaging, require imaging at the subnanosecond scales over an extended area. In this paper, we demonstrate experimentally a time-resolved multispectral acquisition scheme based on single-pixel imaging. Single-pixel imaging is an emerging paradigm that provides low-cost high-quality images. Here, we use an adaptive strategy that allows acquisition and image reconstruction times to be reduced drastically with respect to conventional single-pixel approaches that are based on compressed sensing or full basis scans. Adaptive time-resolved multispectral imaging scheme can have significant applications in biological imaging, at scales from macroscopic to microscopic.

© 2018 Optical Society of America under the terms of the OSA Open Access Publishing Agreement

OCIS codes: (100.7410) Wavelets; (100.3020) Image reconstruction-restoration; (110.1085) Adaptive imaging; (300.6280) Spectroscopy, fluorescence and luminescence; (110.4234) Multispectral and hyperspectral imaging; (170.6920) Time-resolved imaging.

References and links

1. J. Shan and C. K. Toth, *Topographic laser ranging and scanning: principles and processing* (CRC press, 2008).
2. W. Becker, "Fluorescence lifetime imaging - techniques and applications," J. Microsc. **247**, 119–136 (2012).
3. L. Marcu, "Fluorescence lifetime techniques in medical applications," Annals Biomed. Eng. **40**, 304–331 (2012).
4. K. Amarnath, J. Zaks, S. Park, K. Niyogi, and G. Fleming, "Fluorescence lifetime snapshots reveal two rapidly reversible mechanisms of photoprotection in live cells of chlamydomonas reinhardtii," Proc. Natl. Acad. Sci. United States Am. **109**, 8405–8410 (2012).
5. T. Laviv, B. Kim, J. Chu, A. Lam, M. Lin, and R. Yasuda, "Simultaneous dual-color fluorescence lifetime imaging with novel red-shifted fluorescent proteins," Nat. Methods **13**, 989–992 (2016).
6. R. Lussana, F. Villa, A. Dalla Mora, D. Contini, A. Farina, L. D. Sieno, and F. Zappa, "Non-contact inclusion detection in food through a single-photon time-of-flight imager," IEEE Sensors J. **17**, 78–83 (2017).
7. G. Satat, M. Tancik, and R. Raskar, "Lensless Imaging with Compressive Ultrafast Sensing," IEEE Transactions on Comput. Imaging **3**, 398–407 (2016).
8. A. Kirmani, A. Colaço, F. N. C. Wong, and V. K. Goyal, "Exploiting sparsity in time-of-flight range acquisition using a single time-resolved sensor," Opt. Express **19**, 21485–21507 (2011).
9. M. Duarte, M. Davenport, D. Takhar, J. Laska, T. Sun, K. Kelly, and R. Baraniuk, "Single-pixel imaging via compressive sampling," Signal Process. Mag. IEEE **25**, 83–91 (2008).
10. S. S. Welsh, M. P. Edgar, R. Bowman, B. Sun, and M. J. Padgett, "Near video-rate linear stokes imaging with single-pixel detectors," J. Opt. **17**, 025705 (2015).
11. Z. Zhang and J. Zhong, "Three-dimensional single-pixel imaging with far fewer measurements than effective image pixels," Opt. Lett. **41**, 2497–2500 (2016).
12. B.-L. Liu, Z.-H. Yang, X. Liu, and L.-A. Wu, "Coloured computational imaging with single-pixel detectors based on a 2d discrete cosine transform," J. Mod. Opt. **64**, 259–264 (2017).
13. H. Dai, G. Gu, W. He, F. Liao, J. Zhuang, X. Liu, and Q. Chen, "Adaptive compressed sampling based on extended wavelet trees," Appl. Opt. **53**, 6619–6628 (2014).
14. Y.-R. Huo, H.-J. He, F. Chen, and H.-M. Tai, "Adaptive single-pixel imaging based on guided coefficients," J. Opt. Soc. Am. A **34**, 39–51 (2017).

15. F. Rousset, N. Ducros, A. Farina, G. Valentini, C. D'Andrea, and F. Peyrin, "Adaptive basis scan by wavelet prediction for single-pixel imaging," IEEE Transactions on Comput. Imaging **3**, 36–46 (2017).
16. J. Ma, "Single-pixel remote sensing," IEEE Geosci. Remote. Sens. Lett. **6**, 199–203 (2009).
17. S. S. Welsh, M. P. Edgar, R. Bowman, P. Jonathan, B. Sun, and M. J. Padgett, "Fast full-color computational imaging with single-pixel detectors," Opt. Express **21**, 23068–23074 (2013).
18. C. M. Watts, D. Shrekenhamer, J. Montoya, G. Lipworth, J. Hunt, T. Sleasman, S. Krishna, D. R. Smith, and W. J. Padilla, "Terahertz compressive imaging with metamaterial spatial light modulators," Nat. Photonics **8**, 605–609 (2014).
19. E. Tajahuerce, V. Durán, P. Clemente, E. Irles, F. Soldevila, P. Andrés, and J. Lancis, "Image transmission through dynamic scattering media by single-pixel photodetection," Opt. Express **22**, 16945–16955 (2014).
20. Y. Zhang, M. P. Edgar, B. Sun, N. Radwell, G. M. Gibson, and M. J. Padgett, "3d single-pixel video," J. Opt. **18**, 035203 (2016).
21. Q. Pian, R. Yao, N. Sinsuebphon, and X. Intes, "Compressive hyperspectral time-resolved wide-field fluorescence lifetime imaging," Nat. Photonics **11**, 411–414 (2017).
22. Q. Pian, R. Yao, L. Zhao, and X. Intes, "Hyperspectral time-resolved wide-field fluorescence molecular tomography based on structured light and single-pixel detection," Opt. Lett. **40**, 431–434 (2015).
23. A. Farina, M. Betcke, L. di Sieno, A. Bassi, N. Ducros, A. Pifferi, G. Valentini, S. Arridge, and C. D'Andrea, "Multiple-view diffuse optical tomography system based on time-domain compressive measurements," Opt. Lett. **42**, 2822–2825 (2017).
24. C. D'Andrea, D. Comelli, A. Pifferi, A. Torricelli, G. Valentini, and R. Cubeddu, "Time-resolved optical imaging through turbid media using a fast data acquisition system based on a gated ccd camera," J. Phys. D: Appl. Phys. **36**, 1675–1681 (2003).
25. S. Mallat, *A Wavelet Tour of Signal Processing, Third Edition: The Sparse Way* (Academic Press, 2008), 3rd ed.
26. F. Rousset and N. Ducros, *SPIRIT* (https://www.creatis.insa-lyon.fr/~ducros/WebPage/spirit.html, 2017).
27. I. Van Stokkum, D. Larsen, and R. Van Grondelle, "Global and target analysis of time-resolved spectra," Biochimica et Biophys. Acta - Bioenerg. **1657**, 82–104 (2004).
28. P. Peronio, I. Labanca, G. Acconcia, A. Ruggeri, A. A. Lavdas, A. A. Hicks, P. P. Pramstaller, M. Ghioni, and I. Rech, "32-Channel Time-Correlated-Single-Photon-Counting System for High-Throughput Lifetime Imaging," Rev. Sci. Instruments **88,** 083704 (2017).

1. Introduction

Imaging phenomena that occur at (sub)nanosecond time scales have a variety of applications that range from lidar to fluorescence lifetime imaging (FLIM). To obtain lidar distance maps with centimeter resolution, there is the need for measurements at a resolution of some tens of picoseconds [1]. For the recovery of FLIM fluorescence lifetime maps, fluorescence decay needs to be measured on the picosecond to nanosecond time scale. FLIM is one of the most important techniques in biological and materials studies [2, 3], as it can provide fundamental insight into local variations in pH, temperature, and ion concentrations. Beyond this temporal resolution, acquisition of the emission spectrum is fundamental to study photophysical properties of samples that can range from materials to devices [4]. Moreover, spectroscopic information can be used to discriminate between different chromophores in a sample (e.g., biological labeling) [5]. Thus, there is a strong need for multi-dimensional (i.e., temporal, spectral, spatial) FLIM set-ups with picosecond resolution.

Time-resolved multispectral imaging (from tens of picoseconds to nanoseconds) generally relies on a point detector or a linear array coupled to a spectrometer and a time-correlated single-photon counting (TCSPC) board. Building an image requires translation of the sample, or its optical scanning. Although coming at a much higher cost, a streak camera detector allows temporal and spectral information to be acquired for each point with excellent temporal resolution (a few picoseconds), which can then be coupled with a scanning system. By not including the spectral information, one-dimensional (1D) imaging (i.e., along a line) can be acquired, and spectral information can be obtained by sequential measurement of images at different emission wavelengths. Intensified charge-coupled devices equipped with electronic gating that acts as a fast shutter are 2D imagers that allow direct acquisition of a gated image. However, they have lower temporal resolution due to the limited instrumental response function (greater than a

few hundreds picoseconds) and a limited number of temporal and spectral points given by the serial acquisition of the gated and spectral images, respectively. Single-photon avalanche diodes arrays are low-cost systems with ~50-ps time resolution, but they have limited spatial resolutions (~ 32×32 pixels), low filling factors (<5%), and long readout times [6].

During the last decade, the advent of compressed sensing theory led to the emergence of new imager architectures, which include the single-pixel camera (SPC) [7, 8]. The 2D imaging capabilities of a SPC are due to exploitation of a 2D spatial light modulator (SLM) coupled with a single-point detector. A SPC essentially measures the inner product of the scene and a sequence of SLM patterns. Through the post-processing of the resulting dataset, the image of the scene can be recovered [9]. Strategies for SPC image recovery include compressed sensing, basis scans, and adaptive basis scans. While compressed sensing theory provides an excellent theoretical framework for single-pixel imaging, it requires a time-consuming image reconstruction step. Basis scans on a predetermined basis (e.g., Hadamard, Fourier, discrete cosine transform) benefit from rapid inverse transformation for image reconstruction [10–12], but they suffer from long acquisition times. Like basis scans, adaptive basis scans benefit from rapid image recovery, but as only the most significant SLM patterns are acquired, they have much shorter acquisition times – or improved image resolution for a given acquisition time [13–15].

Systems based on SPCs have been shown to be suitable for a wide range of applications, such as remote imaging, hyperspectral imaging, and video acquisition [16–21]. As a consequence, there has been increasing interest in both the signal processing and the optics communities, particularly also due to their compactness and low cost, and to the high-quality images they can provide. Interestingly, a significant advantage of SPCs over the traditional architecture is seen for time-resolved imaging. Indeed, coupling of the point detector of a SPC with a TCSPC board [22, 23] can provide in a low-cost time-resolved system with higher temporal resolution compared to time-gated intensified charge-coupled device cameras [24]. Moreover, as recently shown, addition of a spectrometer and a time-resolved linear detector then provides a time-resolved hyperspectral imager [21].

In this paper, we describe a multispectral time-resolved SPC system that exploits an adaptive acquisition strategy. In particular, as the SLM patterns are adapted to the scene, the image resolution is improved and the acquisition time is reduced. We demonstrate this approach experimentally by imaging the propagation of a laser pulse in a fluorescent solution, and by performing FLIM measurements. Section 2 gives the mathematical modeling of the time-resolved multispectral SPC acquisitions and presents our adaptive acquisition strategy, which we refer to as 'adaptive basis scan by wavelet prediction' (ABS-WP). Moreover, Section 2 presents the experimental set-up, along with the phantom considered. Section 3 reports on the associated experimental results, with some discussion. Finally, our conclusions are reported in Section 4.

2. Material and methods

2.1. Experimental set-up

The experimental set-up is illustrated in Fig. 1. This includes a pulsed supercontinuum laser source (SuperK Extreme EXW-12; NKT Photonics) with an adjustable repetition rate (2-80 Mhz) and a power of up to 1200 mW in the visible spectral range. The repetition rate of the pulsed laser is chosen as 40 MHz. A tunable wavelength filter (SuperK Select; NKT Photonics) is coupled to the laser to select the correct wavelengths for illumination of the object. The spatial light modulator is a digital micro-mirror device (DMD). In particular, the image of the object is formed on a 1024×768 DMD (DLP7000-V7001; Vialux) via *Lens 1* (f = 60 mm). The light that is reflected from the DMD is collected via *Lens 2* (f = 25 mm), which focuses the light onto a 5-mm-diameter fiber bundle that goes to the spectrometer through a 1×10 mm^2 rectangular entrance slit. The spectrometer is composed of a diffraction grating (600 lines/mm) that disperses the light into $\Lambda = 16$-channel photomultiplier detectors (PML-16-1; Becker & Hickl GmbH).

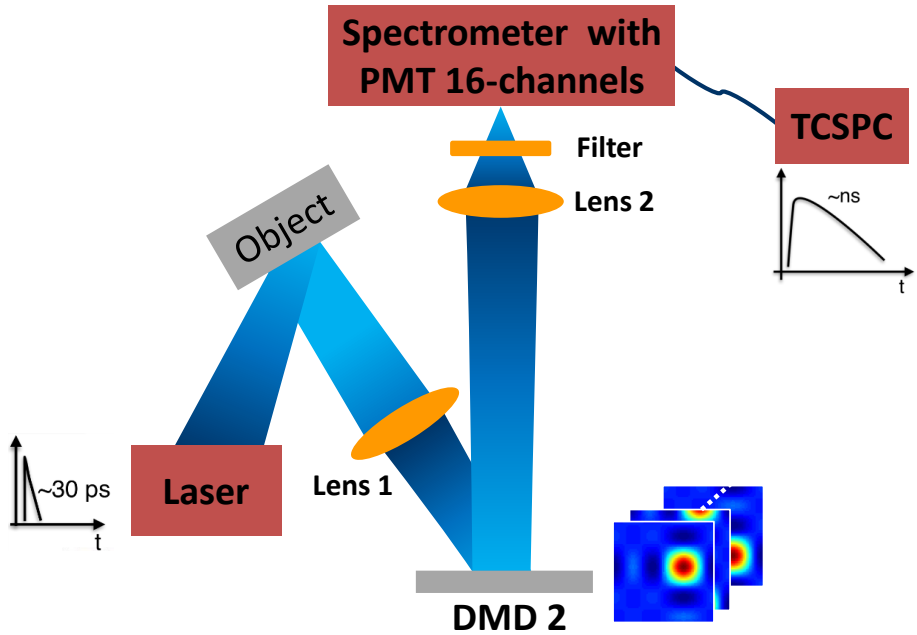

Fig. 1. Experimental set-up. The object is illuminated in reflectance geometry and the light emerging from the DMD is collected by a multispectral time-resolved detector.

The 16 spectral channels range from 505 ± 5 nm to 655 ± 5 nm, with a 10-nm step. The TCSPC board (SPC-630; Becker & Hickl GmbH) with 4096 time channels is coupled to the detectors. To adaptively acquire the dataset, the in-house software alternates between two programs: a Matlab program that processes the data and predicts the next DMD patterns to acquire; and a Labview program that controls the set-up acquisition. To increase the signal-to-noise ratio, the TCSPC time channels are binned, so as to have $T = 60$ time channels that range from 0 ns to 18.00 ns.

2.2. Sample preparation

Two samples are considered. First, two cuvettes are imaged, which are filled with Coumarin 540 (excitation peak, 460 nm; emission peak, 505 nm) and the laser dye DCM (excitation peak, 468 nm; emission peak, 624 nm) dissolved in ethanol. Secondly, another sample is imaged, as depicted in Fig. 3(a). This sample contains three regions that have different temporal and spectral characteristics. Each region has a different shape, which simplifies their identification on the image. The diameter of the circle is 1 cm, the sides of the square are about 1 cm, and the wave is 2.3 cm long and 0.7 cm wide. The circle region contains the laser dye (DCM) deposited on white paper, the square region is made of red fluorescent plastic (excitation peak, 520 nm; emission peak, 625 nm), and the wave region is made of green fluorescence plastic (excitation peak, 464 nm; emission peak, 525 nm). Based on these characteristics, the excitation wavelength band of 470 nm to 490 nm is selected, and a long-pass filter (FEL500; ThorLabs) is added between *Lens 2* and the spectrometer, to filter out the excitation light.

2.3. Image acquisition, reconstruction, and analysis

Multispectral time-resolved imaging provides a 4D map $F(x, y, \lambda, t)$, where (x, y) are the spatial coordinates, λ is the wavelength, and t is the time. We denote $\mathbf{F} \in \mathbb{R}^{D\times\Lambda T}$ as the discrete 4D cube, where D is the number of pixels, Λ is the number of spectral bins, T is the number of time

channels, and $\mathbf{f}_{\lambda,t} \in \mathbb{R}^{D\times 1}$ is the image in the λ-th spectral channel and t-th time channel. Here,

$$\mathbf{F} = \left(\mathbf{f}_{1,1}, \ldots, \mathbf{f}_{\lambda,t}, \ldots, \mathbf{f}_{\Lambda,T}\right). \tag{1}$$

We denote $\mathbf{m}_k \in \mathbb{R}^{1\times\Lambda T}$ as the signal measured for the k-th SLM pattern $\mathbf{p}_k \in \mathbb{R}^{D\times 1}$. For a sequence of K patterns $\mathbf{P} = (\mathbf{p}_1, \ldots, \mathbf{p}_K) \in \mathbb{R}^{D\times K}$, the measurement matrix $\mathbf{M} = (\mathbf{m}_1^\top, \ldots, \mathbf{m}_k^\top, \ldots, \mathbf{m}_K^\top)^\top \in \mathbb{R}^{K\times\Lambda T}$ is experimentally measured. This measures the inner product of the scene and the SLM pattern. Mathematically,

$$\mathbf{M} = \mathbf{P}^\top \mathbf{F} \Delta t. \tag{2}$$

where Δt (in s) is the collection time for a single measurement. The total acquisition time (in s) is $K\Delta t$.

The SPC image reconstruction problem is to invert Eq. (2), i.e., to recover the image $\mathbf{F}$ from the measurements $\mathbf{M}$, with the patterns $\mathbf{P}$ [9] known. In this paper, we use ABS-WP [15] to both design the pattern sequence $\mathbf{P}$ and reconstruct the image $\mathbf{F}$. The SPC directly measures the coefficients of the wavelet transform of the image. As the wavelet transform leads to sparse representation of signals [25], only a few wavelet patterns are required (i.e., $K \ll D$). ABS-WP tracks the location of the significant wavelet coefficients during the acquisition. It first acquires a coarse approximation of the image, and then it predicts and acquires details at increasing resolutions. The prediction step is performed on intensity measurements (i.e., after spectral and temporal integration of the raw measurements). The user controls the image compression ratio (CR $= 1 - K/D$) through simple parameters. This implementation is based on the open-source SPIRIT toolbox [26].

The 4D cube $\mathbf{F}$ is analyzed using a global data analysis approach [27]. First, the 4D cube is integrated over the spatial coordinates and a singular-value decomposition is performed, to determine the number of significant temporal components. Then, the data are fit to the multi-exponential model,

$$F(\lambda, t) = \sum_{m=1}^{M} A_m(\lambda) \exp\left(-\frac{t}{\tau_m}\right), \tag{3}$$

where M is the number of exponential components in the image, A_m is the spectra of the m-th component, and τ_m is its lifetime.

3. Results and discussion

To demonstrate the imaging capability of the system proposed here, a light beam selected from a supercontinuum source ($\lambda = 480$ nm) excites two cuvettes that are positioned side by side and are filled with Coumarin 540 and DCM. The excitation optical path is perpendicular to the cuvettes. Figure 2 shows three different time-resolved acquisitions (with no spectral resolution here). Figure 2(a) is a full basis scan on a 32×32 Le Gall wavelet basis, which requires $K = 32 \times 32 = 1024$ measurements. Figures 2(b) and 2(c) are recovered using an adaptive scan with 64×64 Le Gall wavelet patterns. All patterns have been acquired for $\Delta t = 1$ s. The compression rate is set to a compression ratio of 75% in Fig. 2(b), and to 85% in Fig. 2(c), which leads to 1024 and 614 measurements, respectively. A full basis scan with 64×64 patterns would require $K = 64 \times 64 = 4096$ measurements. This shows that an adaptive strategy is of great importance, to improve image resolution while lowering total acquisition time.

Then, to demonstrate the spectral and temporal capabilities of this set-up, the sample shown in Fig. 3(a) is imaged. The continuous-wave image is first analyzed, as recovered from the raw data integrated over t and λ. In this experiment, Δt was set to 2 s. Figures 3(b)-3(e) show the different continuous-wave images obtained during the acquisition using the ABS-WP technique. Here, the SLM patterns are chosen among a Daubechies wavelet basis, and the compression rate is set to a compression ratio of 93%.

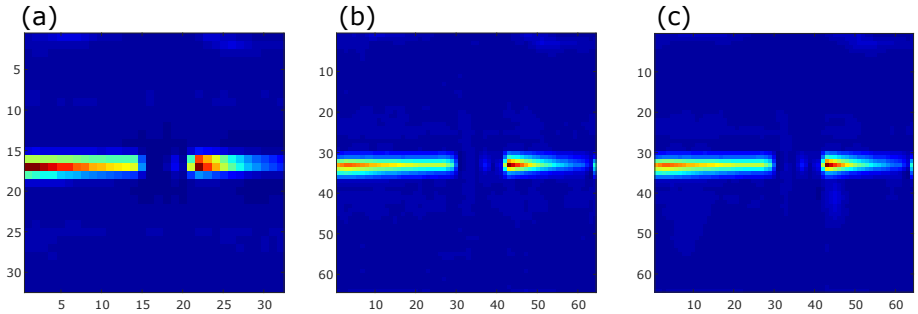

Fig. 2. Time-resolved imaging of a laser pulse that propagates in two adjacent cuvettes, filled with Coumarin 540 and DCM. (a) Full basis scan acquisition of a 32×32 image (1024 measurements). (b, c) Adaptive acquisitions of a 64×64 image using adaptive basis scan by wavelet prediction with compression ratios of 75% (1024 measurements) (b) and 85% (614 measurements) (c). Using an adaptive approach, a higher resolution image can be obtained with fewer measurements, compared to a basis scan approach.

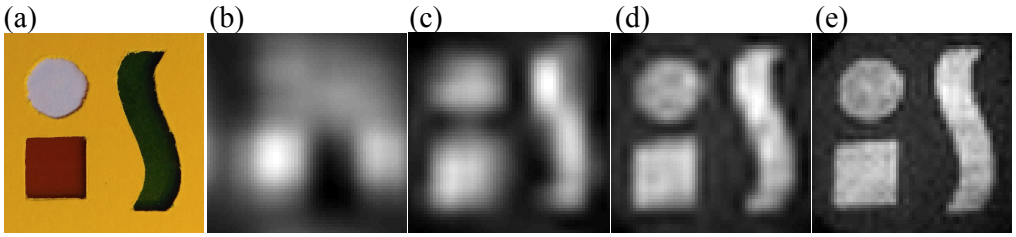

Fig. 3. Adaptive basis scan by wavelet prediction acquistion. (a) Picture of the sample. (b-e) The 64×64 continuous wave images (compression ratio, 93%) recovered during the acquisition, after 16 measurements (b), 64 measurements (c), 227 measurements (d), and 286 measurements (e).

Then, we analyse the spectral and time-resolved images that are recovered by integration of the raw data over t and λ, respectively. With a compression rate as high as 93%, this adaptive set-up allows temporal and spectral stacks to be acquired with very good image resolution. The three different regions of interest (i.e., circle, square, wave) can be easily identified. Figure 4 shows the 64×64 images that are acquired in different spectral and time channels. In the spectral images of Figs. 4(a)-4(c), only the wave stands out in the $\lambda = 525$-nm wavelength channel, and it disappears in the $\lambda = 625$-nm wavelength channel. The situation is the other way around for the square and circle shapes, which is consistent with the excitation and emission peaks of the fluorophores. Moreover, the time-resolved images in Figs. 4(d)-4(f) show that the fluorescence signal decays much faster in the circle region than in the other two regions.

Figure 5 shows how the fluorescence signal behaves spectrally (Fig. 5(a)) and temporally (Fig. 5(b)) in each of the regions of interest. Each of the dotted vertical lines in Fig. 5 corresponds to an image shown in Fig. 4. The temporal curves of Fig. 5(b) all decay exponentially, with a rate that is much faster for the circle than for the other two regions of interest. This is consistent with Figs. 4(d)-4(f), where the circle disappears in the later gates, and with the lifetimes of the fluorophores. Overall, discrimination between these three regions of interest requires both spectral and temporal information.

Finally, we analyze the multispectral time-resolved dataset by adopting the global data analysis approach described in Section 2.3. The singular value decomposition indicates the presence of $M = 3$ temporal dynamics ($\tau_1 = 7.5$ ns, $\tau_2 = 1.3$ ns, $\tau_3 = 0.4$ ns). This corresponds to three

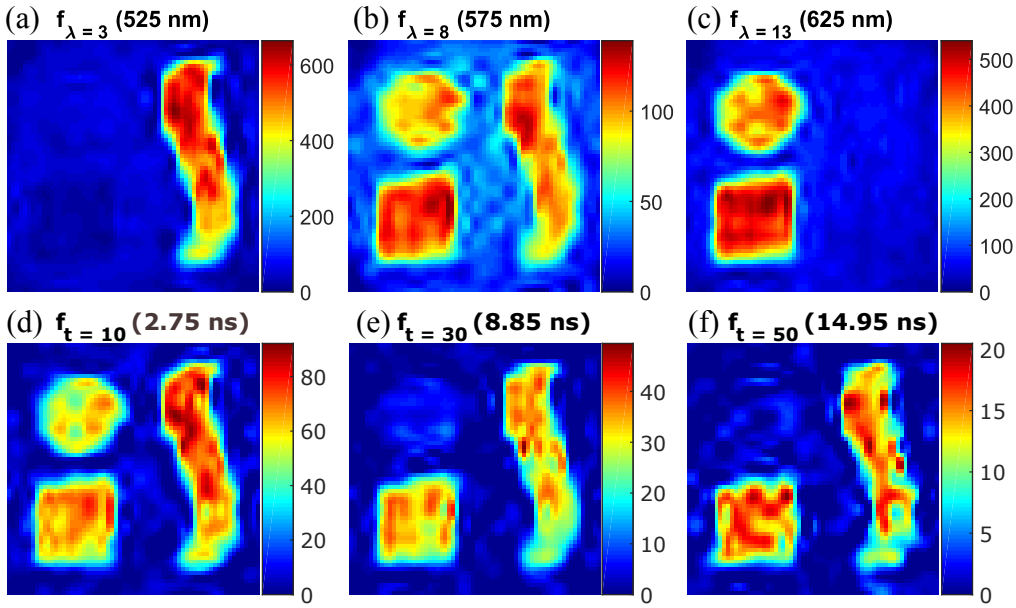

Fig. 4. Spectral and temporal fluorescence images recovered using an adaptive scan (compression ratio, 93%). (a)-(c) Spectral images in different channels. (d)-(f) Time-resolved images in different time channels.

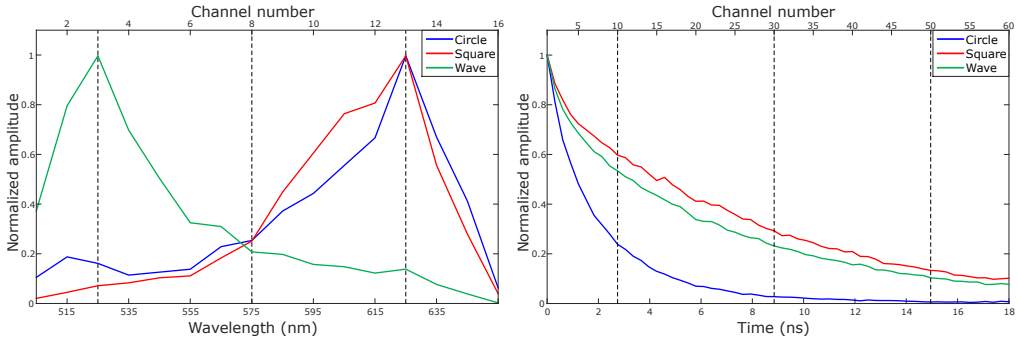

Fig. 5. Spectra (left) and temporal (right) decay in each of the three regions of interest. The dotted vertical lines correspond to the time/ wavelength channels of the images shown in Fig. 4.

decay-associated spectra ($A_1(\lambda)$, $A_3(\lambda)$, and $A_3(\lambda)$) that show two peaks at λ_1 = 525 nm and λ_2 = 625 nm, which correspond to the emission peaks of the three chromophores. Afterwards, the multispectral time-resolved data are fitted pixel-by-pixel to Eq. (3), assuming that the lifetimes are in the range $\tau_m \pm 10\%$. Figure 6 shows the amplitude images at λ_1 and λ_2. The square and wave regions of interest are recovered with the same lifetime τ_1 and with different emission peaks. The intermediate decay τ_2 is strongly present at λ_2. Finally, the fastest decay τ_3 has a negligible contribution to all of the images, and it probably originates from the instrumental response function. These results show that the three regions of interest can be recovered without any a-priori knowledge of the images.

In this study, a time-resolved multispectral imaging system based on an adaptive SPC framework is proposed and validated experimentally. As already shown is [15] for continuous wave images,

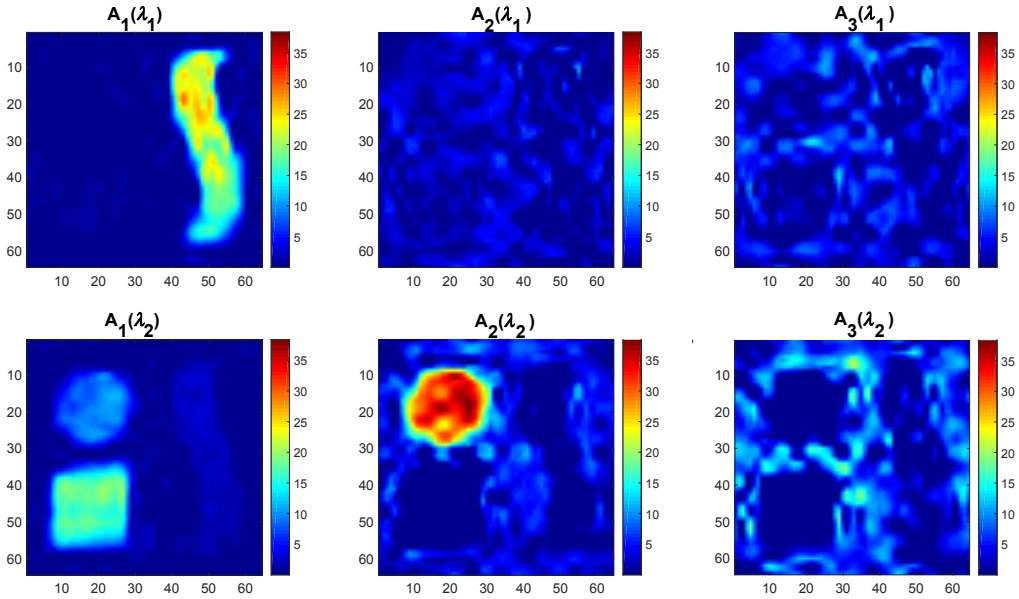

Fig. 6. Images of the decay-associated spectra A_1 (left images), A_2 (middle images), and A_3 (right images) for λ_1 = 525 nm (top images) and λ_2 = 625 nm (bottom images).

the use of an *adaptive* technique allows rapid acquisitions with fewer measurements (i.e., high compression rates) and straightforward image restoration. Conventional *nonadaptive* approaches would suffer from long acquisition and image restoration times, especially for high resolution images. Our ABS-WP method significantly reduces the number of patterns by adapting them to the object under view. Predicting the next patterns with the ABS-WP approach requires a few ms, which is negligible with respect to the acquisition time. Setting Δt to 1 s, the full basis scan in [21] requires $64 \times 64 \times 1$ s= 4096 s, while our adaptive basis scan with a compression ratio of 93% requires only $(1 - 0.93) \times 64 \times 64 \times 1$ s = 286 s. Overall, the drastic reduction of the acquisition and reconstruction times provides time-resolved fluorescence spectroscopy that has imaging capabilities, with this generally performed as single points or in homogeneous solutions, to study dynamic processes at the molecular level. Hence, we foresee applications mainly in the field of multispectral FLIM, for the study of biological samples at microscopic (cellular) and macroscopic (tissue) levels. The main limitation of the system is the shared count-rate among the 16 channels. Great improvements in terms of acquisition time and signal-to-noise ratios can be obtained from the use of a parallel detector, with each unit equipped with its own TCSPC electronics [28], which allows the photon counting Poisson limit ($\sim$ 5% of the laser repetition rate) to be reached on each detector. Finally, it is worth noting that a strong bond between algorithm and system development is a crucial aspect to fully exploit the capabilities of compressive imaging.

4. Conclusion

In this paper, we experimentally demonstrate time-resolved multispectral imaging by means of a SPC using an adaptive scheme. The experiments were performed on samples with fluorophores that have different emission spectra and lifetimes. With a compression rate as high as 93%, this set-up recovers spectrally and temporally resolved images that can discriminate between the different fluorophores. Overall, single-pixel acquisition represents a good trade-off between spatial, temporal, and spectral resolutions. An adaptive strategy such as the adaptitve basis scan by wavelet prediction is motivated by the speed of acquisition. This multi-dimensional approach

represents an important asset for biological imaging of tissues, and for microscopy.

Funding

Université Franco-Italienne (C3-43); French National Research Agency (ANR) (ARMONI project ANR-17-CE19-0003, LABEX PRIMES ANR-11-LABX-0063 of Université de Lyon within the program "Investissements d'Avenir" ANR-11-IDEX-0007); LASERLAB-EUROPE (grant agreement no. 284464, EC Seventh Framework Programme); Starting Grant SOLENALGAE (ERC-2015-StG No. 679814).

Acknowledgments

The experimental data presented in this manuscript were obtained at the Politecnico di Milano thanks to a travel grant for F. Rousset that was provided by the ExploRA'Doc programme of the Région Rhône-Alpes.